Eng. Sci., 2022, **17**, 70–82

Engineered Science
DOI: https://dx.doi.org/10.30919/es8d528

Cellulose Acetate-Hydroxyapatite-Bioglass-Zirconia Nanocomposite Particles as Potential Biomaterial: Synthesis, Characterization, and Biological Properties for Bone Application

Nuha Al-Harbi,[1, 2,] Mahmoud Ali Hussein,[3, 4] Yas Al-Hadeethi[1*] and Ahmad Umar[5, 6*]

Abstract

Biopolymer nanocomposites based on cellulose acetate, hydroxyapatite, bioglass, and zirconia have been synthesized using a solvent-casting method for biological interest. Different concentrations of zirconia have been prepared and characterized. The results clarified that the increase in the concentration of ZrO_2 improves the mechanical properties as the microhardness becomes 405.5 MPa with 11.76 wt% of ZrO_2 instead of 69.4 MPa with no ZrO_2 content. Additionally, introducing ZrO_2 into the nanocomposite improves its wettability as the contact angle is decreased from 65° for the pure sample to 38.4° for the composite with 1.3 wt% ZrO_2. Moreover, the agar diffusion antimicrobial study showed that only the sample with 3.22 wt% of ZrO_2 nanocomposite has mild inhibitory responses against *Pseudomonas aeruginosa*, whereas the rest of the formula does not have any antibacterial activity. Furthermore, the *in-vitro* cytotoxicity of the nanocomposite samples on the Vero cell line was also studied. These Vero normal cells were incubated with test materials for 72h at 37°C/ 5% CO_2, and cell viability was detected using the sulforhodamine B (SRB) assay. All Nanocomposites were mild to non-cytotoxic to Vero cells with high concentration compared with the inhibitory effect of doxorubicin, which was added at 10-fold lower than nanocomposites. With these findings, the proposed nanocomposite could be used in dental applications.

Keywords: Zirconia; Biopolymer nanocomposite; Mechanical properties; Antimicrobial Activity; Cytotoxicity.
Received: 12 August 2021; Revised: 11 September 2021; Accepted: 11 September 2021.
Article type: Research article.

1. Introduction

Bone problems due to trauma, illness, or surgery are a significant major issue with an increasing global population. In the coming years, regenerative medicine and the rising use of dental implants and replacements are projected to hit tremendous levels and could reach 20% of the elderly by 2050.[1] A variety of criteria must be fulfilled for the material utilized as a bone scaffold,[2] including biocompatibility,[3] biodegradation with vanishingly small toxicity,[4] sufficient porosity and mechanical characteristics, and the capacity to be incorporated into biological molecules or tissue regeneration.[5–7]

Bioactive glass (BG) is commonly considered an inorganic filler or additive in biopolymer composites.[8] Therefore, BGs have excellent surface area resulting in a higher rate of dissolution and, as a result, faster apatite creation.[9] Subsequently, the mechanical characteristics of these composites for natural bones are shown to increase as well as provide biomimetic nano-structuring that enhances cell adhesion. The bioactive properties of glass are highly influenced by the composition and shape of glass as well as synthesis methods and the dissolutive rate of ionic

---

[1] *Department of Physics, Faculty of Science, King Abdulaziz University, Jeddah 21589, Kingdom of Saudi Arabia.*
[2] *Department of Physics, Umm AL-Qura University, Makkah, Kingdom of Saudi Arabia.*
[3] *Department of Chemistry, Faculty of Science, King Abdulaziz University, Jeddah 21589, Kingdom of Saudi Arabia.*
[4] *Department of Chemistry, Faculty of Science, Assiut University, Assiut 71516, Egypt.*
[5] *Department of Chemistry, Faculty of Science and Arts, Najran University, Najran-11001, Kingdom of Saudi Arabia.*
[6] *Promising Centre for Sensors and Electronic Devices (PCSED), Najran University, Najran-11001, Kingdom of Saudi Arabia.*
**Email:* ahmadumar786@gmail.com (Prof. Ahmad Umar);
yalhadeethi@kau.edu.sa (Prof. Yas Al-Hadeethi)

dissolution.[10] Due to poor mechanical properties, as being very brittle, the glass structure is not suitable for manufacturing porous scaffolds. Therefore, to enhance their mechanical properties, there is a need for adding BG with biopolymer and metal oxides.[11] Skallevold *et al*.,[10] reported the use of BG in different dental applications such as bone grafting, enamel re-mineralization, dentin hypersensitivity, air abrasion, restorative materials, pulp capping, root canal therapy, bone regeneration, periodontics, and in implant dentistry.

Moreover, nanoparticles have been used in the creation of regenerative composite structures, such as the inclusion of materials containing nanometal oxides. In addition, dental adhesives were also integrated with nanoparticles.[12,13] The nanocomposites are made up of composites containing nanometric dimensional filler particles (less than 100 nm).[14] In addition, several experimental studies have shown that nanoparticle dispersion plays an important role in enhancing the physical – particularly the mechanical properties of composites.

Furthermore, Cellulose acetate (CA) and hydroxyapatite (HAP) composite have been hypothesized to be promising bioactive covering substances used throughout long-term biomedical implants.[15] CA is a renewable material that, as a biodegradable, non-corrosive, non-toxic, and biocompatible material, is gradually drawing researchers' attention due to its potential benefits. It is usually used as a dispersing agent and to distribute nanoparticles evenly in a solution.[16] HAP is similar in composition to the mineral component of bones and hard tissues in mammals. HAP is a filler with the molecular formula of $Ca_{10}(PO_4)_6(OH)_2$. It is a white powder with a needle shape and an average size ranging from 80 to 100 nm and width = 15 ± 25 nm.[17]

BGs are given considerable importance because of their ability for biomedical applications such as enhancing the bond strength in bone formation, speeding healing time, *etc*.[18] These factors have made them a promising choice to be used as a coating on suitable substrates such as ZrO_2-based for biomedical applications. In other words, to achieve the desired implant dental treatment, Zhang and Le developed new ZrO_2/BG composites with excellent mechanical and bioactivity features.[18] In addition, Odermatt *et al.* reported that the nanosized BG particles improve the alkalizing ability of the composite while having a little adverse effect on their specific properties.[19]

Hence, because of its non-toxic properties, chemical stability in the human body, and good mechanical properties, ZrO_2 is commonly used in orthopedics. ZrO_2 is a metal oxide with a white color, excellent strength, and resistance to corrosion that is an example of high ceramic material and particularly biocompatible implant material.[20] Also, high thermal stability, low thermal conductivity, high fracture durability, and relatively high ion conductivity are indeed benefits of ZrO_2.[21] Therefore, ZrO_2 is a broad material in the field of dentistry. Currently, the high strength of ZrO_2 means that it is difficult to process and shape.[22] Nano- ZrO_2 reinforcement of the repair material can dramatically boost the transverse strength of several broken denture polymers as reported by Gad *et al.*[23] In addition, Bacakova *et al.* reported that ZrO_2 nanoparticles have non-toxicity properties.[24] Kumar *et al.* observed that the mechanical performance and thermal properties of the scaffolds are improved by adding ZrO_2 nanoparticles into the BG matrix, and the scaffolds have acceptable antibacterial capabilities against certain bacterial strains.[25] They suggested that it's a great tissue engineering replacement. Additionally, An *et al.* reported that the ZrO_2-HAP composite scaffold has good mechanical features and cellular/tissue compatibility, making it a suitable candidate for large-scale bone restoration as well as regeneration.[26] Moreover, when ZrO_2-HAP-BG was utilized, Bian *et al.*[27] found that the scaffold obtained outstanding mechanical characteristics, bioactivity, and strong cytocompatibility. The composite scaffold represents the potential to be used as a bone implant in the near term.

The objective of this study has been oriented mostly on the impact of ZrO_2 nanoparticles in various proportions on the physical properties of dental composites. It is a spherical-like shape with an average size of 25 nm. Five composite samples comprising 0, 1.3, 3.2, 6.3, and 11.76 wt% of different ZrO_2 nanoparticles were combined with a matrix (where the CA wt% is two times the BG-HAP wt%) and characterized using different methods. Then, the contact angle, and the mechanical and bioactivity properties of the composite with different concentrations of ZrO_2 are explored.

2. Materials and Methods

2.1. Materials

All the chemicals are of analytical grade purity. We purchased CA powder from PDH Company, United Kingdom (UK) and BG nanoparticles (BGNPs), and HAP nanoparticles (HAPNPs) from NanoTech Company Limited Egypt. ZrO_2 nanoparticles (ZrO_2NPs) were purchased from PDH Company, United Kingdom (UK). They have a spherical geometry and a size of 25 nm. BGs are amorphous non-crystalline solids made mostly of silica-based compounds with modest additions. Moreover, BG has a composition of $45SiO_2–24.5Na_2O–24.5CaO–6P_2O_5$ (wt%).[28] BGNPs (their average size is 5.03 nm) are white powder with a spherical-like shape.

2.2. Preparation and fabrication of CA-HAP-BG-ZrO_2 nanocomposites

Initially, the process involving the determination and evaluation of the weight fractions needed for a suitable composite is as the following: CA was dissolved in 10 mL of acetone and continuously stirred for 10 min at a temperature of 50 °C. A sample of 100 wt% of CA is considered a pure sample. Then, the nanofillers were poured into the CA that had dissolved. Moreover, using a tabletop ultrasonic cleaner, the mixture was sonicated to ensure the proper uniform mixing and dissolution of the filler in the polymer matrix (CA). The

Table 1. The different weight fractions, compositions, and densities of CA-HAP-BG-ZrO_2 NPs.

Sample #	Compositions	Density (kg/m^3)
Pure	100 wt% CA	1280
CHBZ1	65.8 wt% CA, 16.45 wt% HAPNPs 16.45 wt % BGNPs, 1.3 wt% ZrO_2 NPs	1950
CHBZ2	64.5 wt % CA, 16.13 wt% HAPNPs 16.13 wt% BGNPs, 3.22 wt% ZrO_2 NPs	2215
CHBZ3	62.5 wt% CA, 15.62 wt% HAPNPs 15.62 wt% BGNPs, 6.25 wt% ZrO_2 NPs	2321
CHBZ4	58.82 wt% CA, 14.7 wt% HAPNPs 14.7 wt% BGNPs, 11.76 wt% ZrO_2 NPs	2436

well-mixed composite is then cast into a circular glass dish and was allowed to be set overnight at room temperature, as seen in Fig. S1. The samples with their different weight fractions, compositions, and densities are shown in Table 1.

2.3 Characterization Techniques

The synthesized nanocomposites, previously described, were subjected to structure characterization using different techniques. The physical and chemical properties were evaluated using scanning electron microscopy (SEM), X-ray diffraction (XRD), Fourier Transform Infrared Spectroscopy (FTIR), X-ray photoelectron spectroscopy (XPS), and thermal analysis. A summary of the analysis methods will be described as follows: The phase composition of the ZrO_2/CA/BG-HAPNPs composite was studied by X-ray diffraction analysis (XRD, Bruker D8 advance diffractometer, Germany). The x-ray tube parameters used in this analysis were 40 kV applied voltage and 15 mA beam current with diffraction patterns obtained at 25 °C and over a 20° to 80° angular range. A scanning electron microscope (SEM, Carl-Zeiss Sigma 500 VP, Germany) is used to investigate the morphology of the nanocomposite surface. In this study, the images were acquired at different magnifications at 20-25 keV with the nanocomposite surface coated with a gold/palladium thin alloy film to prevent surface charging and activate the emission of secondary electrons.

Furthermore, the ZrO_2/CA/BG-HAP composite elemental evaluation was carried out using an Energy-Dispersive X-ray (EDX) detector (EDS, EDAX Inc., Mahwah, NJ, USA) linked to the SEM machine. Then, the screened data was post-analyzed using APEXTM EDS software. The surface elemental composition was investigated using X-ray photoelectron spectroscopy (XPS, Perkin Elmer PHI 5600, USA). To classify and quantify the existing elements on the surface of the specimen, large energy spectra of the prepared composites were analyzed over a range of energies of 0–1350 eV. Fourier transform infrared spectrometer (FTIR, Bruker Tensor 27, Germany) was used to identify the functional groups of the synthesized nanocomposites. Its spectral range was 400 to 4000 cm^{-1}, with a resolution of more than 1 cm^{-1}. The thermal analysis of ZrO_2 nanocomposites samples is measured using Shimadzu (TGA-50) Thermogravimetric analyzer. The particle size of synthesized composites dispersion in acetone was recorded by dynamic light scattering (DLS) system using Microtrac Nanotrac Wave. The technique is also referred to as photon correlation spectroscopy (PCS) in which particle size is determined by measuring the random changes in the intensity of light scattered from a suspension or solution. The sample is illuminated by a laser beam followed by the detection of the resultant fluctuations of the scattered light at a known scattering angle θ by a fast photon detector.

2.3.1 Mechanical Properties by Ultrasonic Testing

The mechanical properties were examined using the ultrasonic system (UT) to calculate wave velocities using the pulse-echo technique. These velocities were measured using an ultrasonic flaw detector (SIUI ultrasonic flaw detector) connected to an oscilloscope. In addition, the uncertainty was estimated to be about 9 m/s and 6 m/s for longitudinal and transverse velocities, respectively. For longitudinal waves, oil was used as a coupling medium, while the varnish was used for shear waves. Moreover, the mechanical properties were calculated using the equations in[29,30] with the help of the estimation of shear velocity, longitudinal velocity, and density (Table 1).

2.3.2 Contact Angle Measurements

Contact angle measurements are carried out using the SEO Phoenix-10 contact angle analyzer for different composite samples. Low-bond axisymmetric drop shape analysis (LB-ADSA) plug-in tool for Java image processing; ImageJ software is used for contact angle estimation. In LB-ADSA, the shape-matching adjustment of the droplet image on the sample by shifting their corresponding sliders would expect its shape to be closely matched to the drop image.

2.3.3 Biological Test

2.3.3.1 Antimicrobial Activity Assays

We used a diffusion-growth kinetic technique in agar to assess the antibacterial activity of the synthesized nanocomposites. We concluded this experiment according to Jaramillo *et al.* procedure.[31] A total of five bacterium strains included *P. Aeruginosa*, *E. Coli* (ATCC 25922), *S. Typhi*, *S. aureus* (ATCC 25923), and *B. Subtilis* (ATCC), tested and obtained from Microbial Biotechnology and Molecular Biology lab (Egyptian Atomic Energy Authority, Egypt).

For the antibacterial diffusion growth kinetics on agar test,[32] strains struck separately on Nutrient Agar (NA) medium, followed by incubation overnight at 37 °C. We choose a well-isolating colony within each strain using an inoculating loop, then introduced it to one of the 50 ml falcon tubes that contain 10 ml of Nutrient agar broth. This broth was then incubated at room temperature overnight till its turbidity obtained by a turbidimeter reached “0.5” on McFarland scales. The cells were suspended to 1:10, yielding 107 CFU/mL as the final concentration of inoculum. Every inoculum of the five strains was sown equally on nutrient agar (NA) dishes. After that, every nanocomposite thin sheet (3 mm×3 mm), as well as a CA pure sample, has been attached to the top of TSA plates to confirm good adhesion. The control was placed in the center of the plate, and each one of nanocomposites CHBZ1-4 was placed surrounding the control. Finally, the plates were incubated for 24 hours at room temperature.

2.3.3.2 *In-Vitro* Cell Viability

Four samples of nanocomposites CHBZ1-4 with different concentrations have been tested individually in synchronization with the impact of the CA effect alone. In-vitro cytotoxicity against normal Vero cells (Green monkey kidney cell line) was used.[33] Green monkey kidney has been obtained from (Nawah Scientific Inc., Mukatam, Cairo, Egypt). SRB (Sulforhodamine B) assay was used to determine the Vero cell's viability. The aliquots of 100 µL Vero-cell suspension containing approximately 5×10^3 cells were inserted in 96-well plates and then incubated for one day in DMEM medium. In a humidified, 5% (v/v) CO_2 environment at room temperature, these cells were inserted into 100 units/mL penicillin and 10% heat-inactivated fetal bovine serum. We added 100 µL of media containing 100 ug/ml of nanocomposites CHBZ1-4 to the cells and the cells were exposed for 72 hours to the drug. We treated the samples by replacing the medium with 150 µL of 10% TCA (trichloroacetic acid) before incubation for 1 hour at 4 °C, then TCA sol emptied, and the cells were cleaned five times with ddH_2O. A 70 µL SRB sol (0.4 % w/v) was applied to the cells and allowed to brood for 10 minutes inside the dark conditions at 37 °C. Dishes were rinsed three times with 1 % of acetic acid and then dried overnight. We applied 150 µL of TRIS (10 mM) to solubilize the protein-bound SRB stain and used a Microplate Reader (model ELx800, Biotek, USA) to detect the absorption at 540 nm. We carried out this experiment in parallel with testing the viability of normal cells against 10 ug/ml Doxorubicin (DOX) as a positive control.

3. Results and Discussion

3.1 X-ray Diffraction (XRD) Analysis

XRD measurements of the synthesized nanocomposites are shown in Figs. 1(a-e). The diffractogram of the CA indicates amorphous behavior patterns as shown in Figs. 1(a-e).[34,35] Figs. 1(a-e) shows the XRD patterns of the synthesized nanocomposites with different contents of ZrO_2 ranging from 1.3 to 11.76 wt%, respectively. As a result, all of the samples' diffraction characteristic peaks for ZrO_2 crystals were in strong alignment with the International Center for Diffraction Data (ICDD) (PDF: 49-1642). ZrO_2 has diffraction peak values at 30°, 34°, 50°, and 59°.

Also, Figs. 1(a-e) shows that the main composition in the composites is HAP. It is because there exist the semi-crystalline peaks at 25.9°, 31.8°, 32.0°, 33.0°, and 40.0°, which constitute the structure of HAP crystals, also, this figure shows that most diffraction peaks of BGs appeared as stated as.[36,37] It can be seen that the major components of the composites are still HAP. Generally, the introduction of ZrO_2 into the composites can enhance the decomposition of HAP into tricalcium phosphate (TCP) and CaO because CaO can be incorporated into the ZrO_2 lattice in agreement with.[38] The obtained data from XRD measurements agreed with the obtained data from microhardness measurements. The addition of ZrO_2 nanoparticles into the composites is good for the enhancement of the mechanical performance of the nanocomposites as stated.[39]

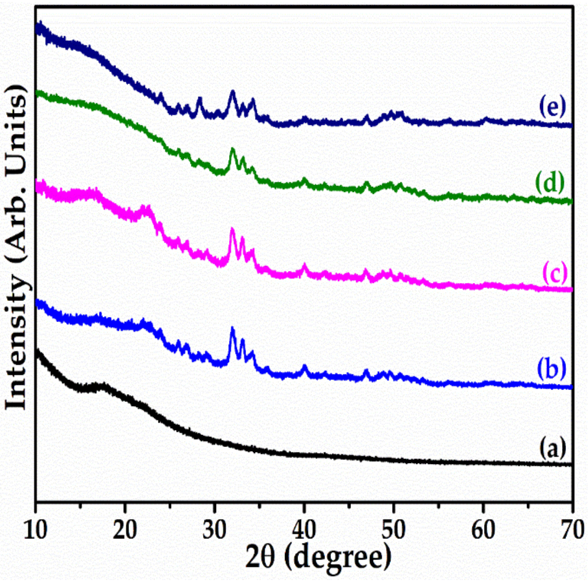

Fig. 1 XRD patterns of the synthesized nanocomposites with different weight percentages of ZrO_2: (a) Pure, (b) CHBZ1, (c) CHBZ2, (d) CHBZ3, and (e) CHBZ4 samples.

3.2 Scanning electron microscopy/energy dispersive X-ray spectroscopy (SEM/EDX) analysis

The observed images of the synthesized nanocomposites are shown in Figs. 2a and 2b. The obtained images of EDX mapping are presented in Figs. 2c and 2d. As shown in Fig. 2(a), the synthesized nanocomposites with 3.22 wt% of ZrO_2 appeared as circular spots distributed uniformly over the entire surface, while the synthesized nanocomposites with 11.76 wt% of ZrO_2 show variation in morphological features and appeared as irregular forms and agglomeration with inter-granular micropores and small amounts of porosity; the ZrO_2 grains were found with lighter color ratios as shown in Fig. 2(b).[40-42] The SEM-EDX analysis was performed to determine the surface elemental composition of the synthesized composites. The elemental mapping for Zr, O, C, P, Ca, Na,

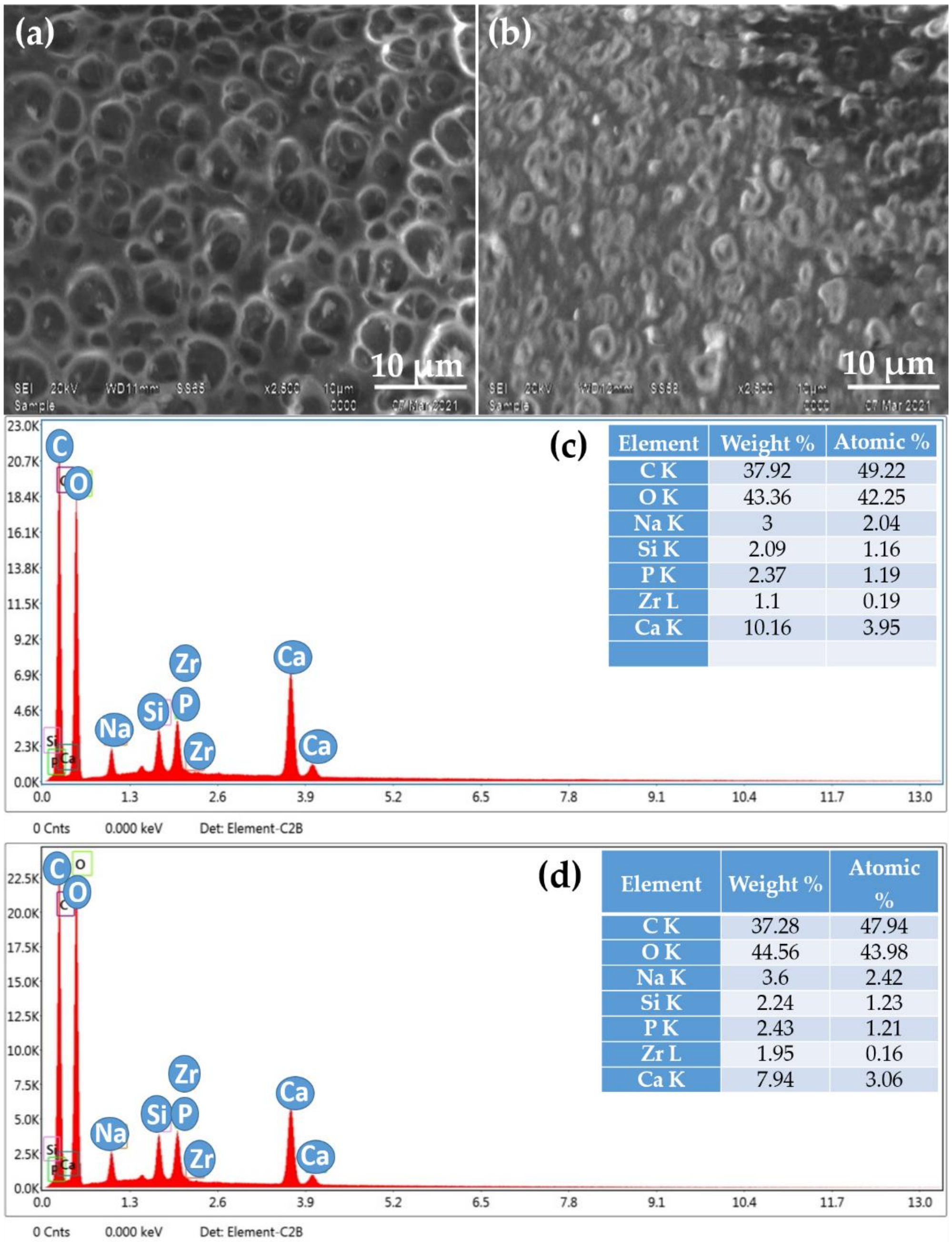

(c)

Element	Weight %	Atomic %
C K	37.92	49.22
O K	43.36	42.25
Na K	3	2.04
Si K	2.09	1.16
P K	2.37	1.19
Zr L	1.1	0.19
Ca K	10.16	3.95

(d)

Element	Weight %	Atomic %
C K	37.28	47.94
O K	44.56	43.98
Na K	3.6	2.42
Si K	2.24	1.23
P K	2.43	1.21
Zr L	1.95	0.16
Ca K	7.94	3.06

Fig. 2 SEM images of the synthesized composites with (a) CHBZ2, (b) CHBZ4, (c) analysis EDX for CHBZ2, and (d) EDX for CHBZ4 samples.

and Si elements for the synthesized composites with 3.22 and 11.76 wt% of ZrO_2 is shown in Figs. S2 and S3. From Figs. S2 and S3, it was observed that all the samples contain Zr, O, C, P, Ca, Na, and Si in certain contents as stated above.[43]

3.3 Dynamic Light Scattering

Dynamic light scattering is popularly used for the determination of the size of particles in suspension, emulsions, colloids, polymers, *etc*. The advantage of this is it allows the particle size down to 1 nm diameter. The acetone-suspended nanocomposite samples were diluted and analyzed by the DLS particle size analyzer. The size distribution of the synthesized composites is in the nano range as presented in Fig. S4. The data reveals that the sizes of the synthesized nanocomposite are in the nanoscale. The average particle sizes are 387, 550, 509, 474, and 984 nm for pure, CHBZ1, CHBZ2, CHBZ3, and CHBZ4 samples, respectively.

3.4 X-ray Photoelectron Spectroscopy

The chemical composition of the surface of the synthesized composites and the states of the material coating were determined by using X-ray photoelectron spectroscopy (XPS), and the obtained data are presented in Figs. 3 (a-d).

The survey-wide energy spectra of applied composites were taken over an energy range of 0–1350 eV to identify and quantify the present elements on the composite surface. A typical XPS spectrum of the CHBZ1 composite is shown in Fig. 3 (a). The plot exhibits seven signals, in this low-resolution spectrum, at 103.59, 190.66, 287.12, 348.25, 133.03, 533.67, and 1072.27 eV. These signals could be attributed to electrons ejected from Si2p, Zr3d, C1s, Ca2p, P2p, O1s, and Na1s orbitals.[44]

While a typical XPS spectrum of CHBZ2 composite is shown in Fig. 3 (b), the plot also exhibits seven signals, in this low-resolution spectrum, at 103.83, 191.11, 287.02, 348.12, 133.96, 533.24, and 1072.27 eV with low shift, respectively in agreement with.[44] Also, typical XPS spectra of CHBZ3 and CHBZ4 composites are shown in Figs. 3c and 3d. The percentage of the different elements present in all nanocomposites was determined and listed in Table 2.

The high-resolution signals, corresponding to these elements, are shown in Fig. 3, the C1s and O1s that represent the main constituents of CA. It is worth noting that the C1s signal while the main peak was detected at 287.12 eV, which could be related to C=O species.[45] It is clarified that the peaks at 103.59 and 1072.27 eV were attributed to Si and Na atoms in the structure of Si–O and Na–O from SiO_2 and Na_2O, respectively of the bioactive glass. In addition, the peak at 348.25 eV was attributed to the Ca atom in the structure of Ca–O of HAP in the composite. Moreover, the peak at 533.67 eV was assigned to the O atom in the structure of O-CO and that is related to metal oxides of Na_2O and ZrO_2, respectively. Thus, it emphasizes the presence of these metals as oxides and other explanations for hydroxyl adsorption present on the composite.[46] Furthermore, the peak at 190.66 eV corresponded to ZrO_2.[47] Therefore, the P2p core level peak located at 133 eV is attributed to P–O bonds in PO_4^{3-} that is present in HAP in agreement with.[43]

3.5 FTIR Analysis

FTIR is considered the most powerful tool to identify chemical bonds (functional groups) and is used to detect possible changes in the functional groups in the structure. The wavelength of absorbed light is characteristic of the chemical

Table 2. The atomic percentage ratio of the elements on the surfaces of CHBZ1, CHBZ2, CHBZ3, and CHBZ4 nanocomposites was measured by XPS.

Concentration	O%	C%	Na%	Ca%	Si%	P%	Zr%
CHBZ1	36.94	54.74	3.12	2.26	1.88	1.05	0.1
CHBZ2	38.11	52.79	3.1	2.73	1.51	1.5	0.26
CHBZ3	39.83	47.94	3.35	3.89	2.84	1.8	0.33
CHBZ4	38.33	52.54	2.97	2.33	1.6	1.55	0.68

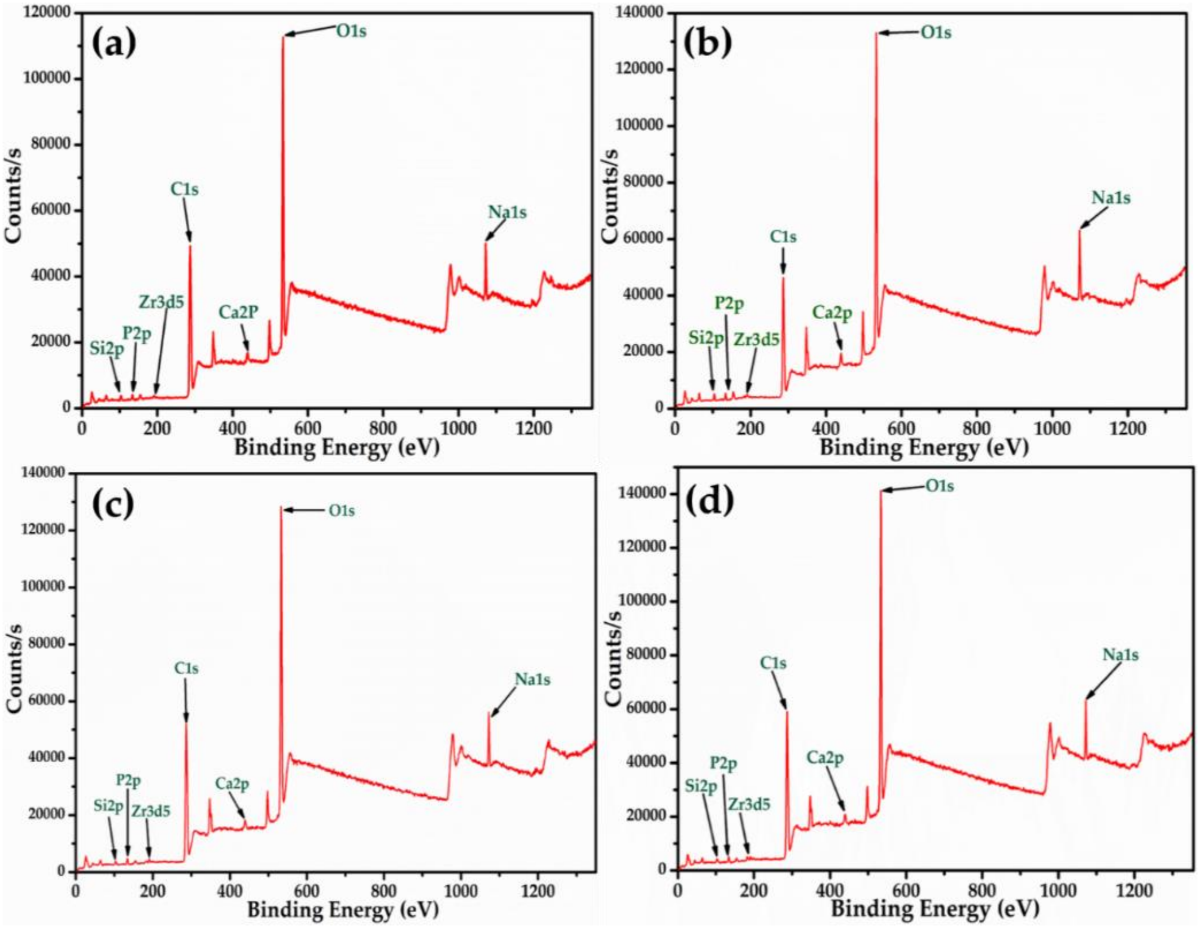

Fig. 3 XPS spectra for (a) CHBZ1, (b) CHBZ2, (c) CHBZ3, and (d) CHBZ4 nanocomposite samples.

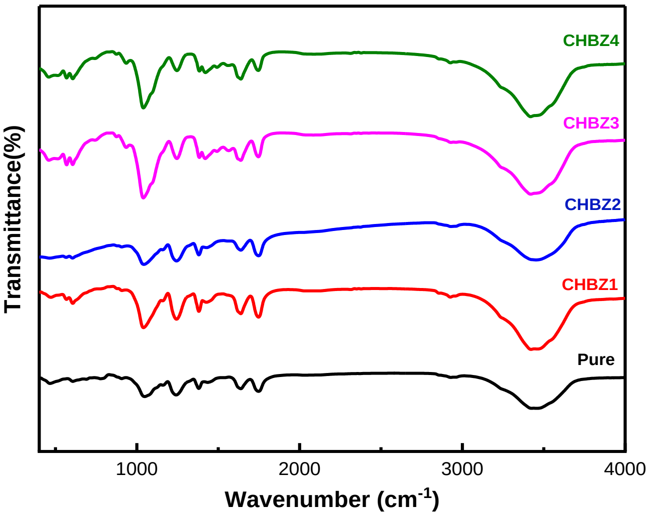

Fig. 4 FTIR spectrum of the synthesized nanocomposites.

bond as can be seen in the spectra throughout the range of 400–4000 cm^{-1}. The FTIR spectra of the synthesized composites are presented in Fig. 4.

The spectra show broad peaks around the wavenumber 3424-3450 cm^{-1} for each spectrum due to the presence of hydroxyl (O–H) groups on the surface of the synthesized composites.[48] In addition, the peaks detected at ~ 2930 cm^{-1} may be due to C–H stretching vibrations of CA in agreement with.[49,50] Moreover, the bands revealed in 1747 and 1639 cm^{-1} could be attributed to the stretching vibrations of carbonyl (C=O) and C=C groups, respectively.[51,52]

Furthermore, the absorption peaks at 1420 and 1380 cm^{-1} correspond to C–H_2 bending vibration of CA.[53] Also, the absorbance bands around 950–1250 cm^{-1} were determined to be the presence of all 6 types of composites which signify the C–H stretching and C–O groups.[53-55] It is clear that these peaks were observed in all spectra with small shifts. The strong interaction between the P–O group and calcium on an appetite surface demonstrates this shift, indicating that these obtained materials are indeed composites.

In addition, absorption bands in the range 600 to 400 cm−1 may be assigned to the metal-oxygen (M–O) as Ca–O, Zr–O, and P–O stretching mode as shown in CHBZ1, CHBZ2, CHBZ3, and CHBZ4 samples. [56–58]

3.6 Mechanical Properties by Ultrasonic Testing

The objective of this section is to evaluate the effects of zirconia nanoparticle addition at low concentrations (up to 12 wt%) to biopolymer on mechanical properties, such as micro-hardness and Young's modulus with the help of ultrasonic technique.

Figure 5(a) shows the effects of the presence of ZrO_2 nanoparticles on the micro-hardness of the synthesized composites. As shown in this figure, the micro-hardness of the synthesized composites increases with the increase of ZrO_2 content and has been improved greatly after introducing ZrO_2 nanoparticles into biopolymer nanocomposites as compared with those of unmodified composites.

It can be observed from this figure; the microhardness is increased from 245.8 MPa at 1.3 wt% to 405.5 MPa at 11.76 wt% of ZrO_2 as compared with the unmodified ones that show low micro-hardness (69.4 MPa).[29] This is because Zirconia has a high flexural strength and micro-hardness, as well as a decrease in porosity. Furthermore, zirconia shows excellent biocompatibility compared to other ceramic materials such as alumina and found.[59,60] Also, the density of the synthesized composites increased from 1280 to 2436 kg/m^3 with increasing ZrO_2 content as shown in Table 1; consequently, the micro-hardness of biopolymer composites was increased.[39] The addition of zirconia in biopolymer between 1.3 wt% and 11.76 wt% zirconia would provide the optimum mechanical properties suitable for denture base applications similar.[29]

Figure 5(b) shows Young's modulus as a function of ZrO2 weight fraction (wt%). It can be detected from this figure that Young's modulus increases from 5181.6 to 6467.3 MPa with increasing ZrO_2 weight fraction from 1.3 to 11.76 wt%, respectively. In other words, Young's modulus increases with the increase in the ZrO_2 weight fraction (wt%).

3.7 Contact Angle Measurements

It is of substantial significance to identify and describe the wettability of solid surfaces for material characterization. The wettability of the solid-fluid surface mechanism is also established by calculating the contact angle shaped between a water droplet and a solid surface.[61] Low wettability and unsatisfied adhesion characteristics also exist on the polymer surface. Therefore, the polymer surface has to be adjusted and controlled. Different fillers and composites with different weight fraction contents are used in this analysis. Wettability is obtained by calculating the liquid drop interface angle with the biopolymer substrate. Low contact angle (<< 90°) refers to high wettability, whereas low wettability is detected for higher contact angle (>> 90°).[62]

The contact angle is carried out using a contact angle analyzer system (model SEO Phoenix-10). It consists of Phoenix 300 instrument and ImageJ software [63] where the measurements were carried out at room temperature (20-25˚C). An HHD camera is used to record a drop image within 10 sec of water deposition. In this study, a low-bond axisymmetric drop shape analysis (LBADSA) plug-in,[64] based on the Young-Laplace equation, is used to measure the contact angle here. This plug-in in ImageJ software calculates the contact angle of a drop image on a flat surface using the ellipse approximation.

Figure 6 shows contact angle (α) images of different weight fractions of ZrO_2 in biopolymer nanocomposite. It is observed that zirconium oxide addition enhances wettability. In other words, the contact angle is decreased from 65° for the pure sample to 38.4° for the composite with 1.3 wt% ZrO_2. This leads to improvement in the hydrophilicity of the biopolymer matrix under the addition of ZrO_2 NPs. However, as ZrO_2 is applied to the biopolymer matrix, an extra hydroxyl group on ZrO_2 and HAPs can begin to bind with water and

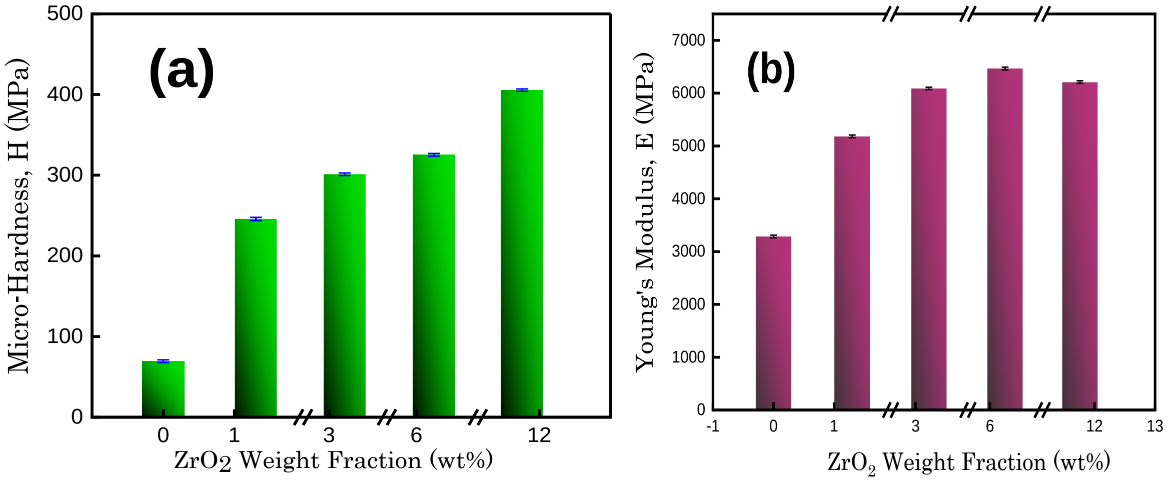

Fig. 5 (a) Micro-Hardness of composites with different weight percentages of ZrO_2 and (b) Young's modulus as a function of ZrO_2 weight fraction (wt%).

increase hydrophilicity.[36]

Furthermore, as shown in Fig. 7, the fraction of ZrO_2 in the nanocomposite polymer has an insignificant effect on the contact angle improvement.

3.8 Thermal Analysis

Measurements of thermogravimetric analysis (TGA) were carried out using a Shimadzu TGA/DTA-50 system from Kyoto, Japan. The phase changes and weight losses of the samples were determined by heating at a range of 10°C.min^{-1} in presence of nitrogen gas to avoid thermal oxidation of the powder sample. The thermal measurements were done up to a temperature of 700 °C, using α-Al_2O_3 as a reference.

The thermal decomposition and thermal stability of polymers are most effectively assessed by TGA. TGA of the synthesized nanocomposites was performed at a temperature ranging from 25 to 700 °C. The obtained thermograms are presented in Figs. S5(a-e). In this figure, the TGA of the pure, CHBZ1, CHBZ2, CHBZ3, and CHBZ4 nanocomposites showed three weight losses on the TGA profile. The first weight loss was observed with rising temperature up to about 220°C. The four composites exhibiting a loss in weight amounted to 6.3, 7.2, 5.5, and 8.5 %, respectively for CHBZ1, CHBZ2, CHBZ3, and CHBZ4 nanocomposites. Also, the first weight loss of the pure CA sample was observed with rising temperature up to ~290°C and amounted to 4.8 %. This loss

Fig. 6 Images of drop on biopolymer nanocomposite under different weight fractions of ZrO_2.

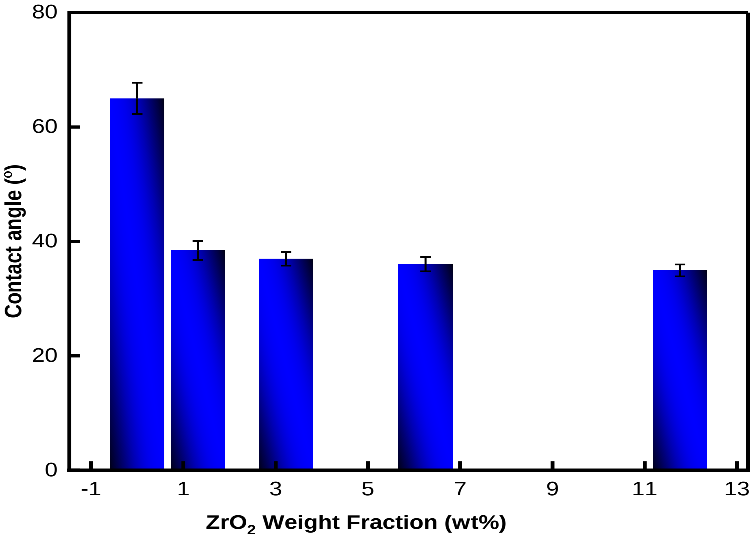

Fig. 7 Contact angle as a function of wt% weight fraction of ZrO_2 on the biopolymer nanocomposite.

could be attributed to the evaporation of loosely bound moisture on the surface and the intermolecular hydrogen-bonded chemisorbed water.[65] The second weight loss is a sharp decrease in weight in a temperature range of 220–350 °C.

This weight loss amounted to ~ 81.7, 48.6, 47.5, 45, and 53 %, respectively for pure, CHBZ1, CHBZ2, CHBZ3, and CHBZ4 nanocomposites and could be thermal depolymerization of hemicellulose acetate and the breakdown of glycosidic linkages of CA.[66] The third weight loss in the temperature range of 350-425 °C amounted to ~ 13.5, 28.1, 26.5, 18.5, and 32 %, respectively for pure, CHBZ1, CHBZ2, CHBZ3, and CHBZ4 nanocomposites and could be attributed to the removal of the residual oxygenated groups, such as hydroxyl, carbonyl, and M-O groups on the surface of the synthesized nanocomposites.[65] Synthesized nanocomposites are stable at a temperature of less than 225 °C.

Also, the synthesized CHBZ3 nanocomposite is more thermally stable compared to the other three composites. In the Differential thermal analysis (DTA or DrTGA) curve, an endothermic peak appeared at 280 - 320 °C, presumably caused by the decomposition of the carbonate groups, and shows the degradation of the nanocomposites.[36] Also, an endothermic peak appeared at 386 - 410 °C, which shows the crystallization would start in composite samples or maybe because of the presence of various oxygen functional groups from its structure with different thermal stabilities and their cleavage occurring at different temperatures.[67]

The TGA results of the synthesized nanocomposites have been tabulated in Table 3, giving clear information on the degradation pathway of these materials. From Table 3, the T_{10} and T_{50} symbols refer to the corresponding temperature where 10% (as the measures of the onset) and 50% (as half degradation temperature) mark the weight losses, respectively. Noticeably, the values of T_{10} and T_{50} show diverse thermal performances according to the loading amounts of ZrO_2.

Great stability was detected for 6.25% loading of ZrO_2 nanocomposite. The final composite degradation temperature (CDT_{final}).[68] As presented in Table 3, is recognized from the TGA curve. The CDT_{final} values take place from 405 °C to 475 °C. Also, PDT_{max} represents the maximum temperature accomplishment when the sample decomposition was recognized.[69] From these findings, it was confirmed that the thermal stability of synthesized nanocomposites was enhanced excellently by the incorporation of proper loading of ZrO_2.

3.9 Effect of Nanocomposite on Vero Cells Viability

All nanocomposites CHBZ1-4 were tested separately *in-vitro* for their cytotoxic activity against Vero cells (Green monkey kidney), and normal cell lines using SRB assay, which runs parallel with examining cells with 10 ug/ml DOX. Table 4 represents the percentage of cell viabilities after treatment with 100 ug/ml of nano formula, where the percentages range between 56.6079 % for CHBZ3 and 79.2287 % in the case of CHBZ4. On the other hand, only 10 ug/ml (only one cell line, for *in-vitro* evaluation. All data showed that mild to non-cytotoxic effects have been seen for the nano formulas tested compared to the inhibitory effect of DOX to cells, although it was added with concentrations 10 folds lower than that of our target nanocomposite to a tenth of the concentration of NCs) of DOX were enough to kill about 96.5% of cells in the same conditions.

Figure 8 represents an image for each cell line after treatment with each formula separately, contrary to the image of cells treated with DOX. Growth inhibition has been seen obviously in the case of DOX, while cell density after the same time and condition seems to be good. This study is designed to investigate the cytotoxicity of novel Nanocomposites CHBZ1-4 on normal cells. We used "Vero cells", the available normal.

3.8 Antibacterial Activity Results

In Fig. 9, the antibacterial examination for the target nanocomposites shows no activity against any of the five pathogenic bacterial strains; only mild inhibitory activity is shown against *P. Aeruginosa* by nanocomposite CHBZ2. Being noble and nearly not active against these already resistant pathogenic bacterial strains or mammalian normal cells never decreases its importance as a potent and safe nanocomposite formula as a dental filler, but it may be highly recommended for use due to its safety properties.

4. Conclusion

In this work, it was concluded that the nanosized composite

Table 3. TGA results of synthesized nanocomposites with different ratios of ZrO_2.

Concentration	Temperature (°C) for different percentage decompositions			
	T_{10}	T_{50}	PDT_{max} (°C)^a	CDT_{final} (°C)^b
CHBZ1	305	344	345	475
CHBZ2	244	360	318	420
CHBZ3	235	356	280	442
CHBZ4	249	396	292	425

^{a} Values are from the DTG curve.

^{b} Values are from the TGA curve.

Table 4. Values of Vero cell viability % after treatment with 10 ug/ml of NCs formulas separately in comparison with treatment with 10 ug/ml DOX.

NCs Formula	CHBZ1	CHBZ2	CHBZ3	CHBZ4	DOX
Cell Viability %	78.334	74.0074	56.6079	79.2287	3.5673

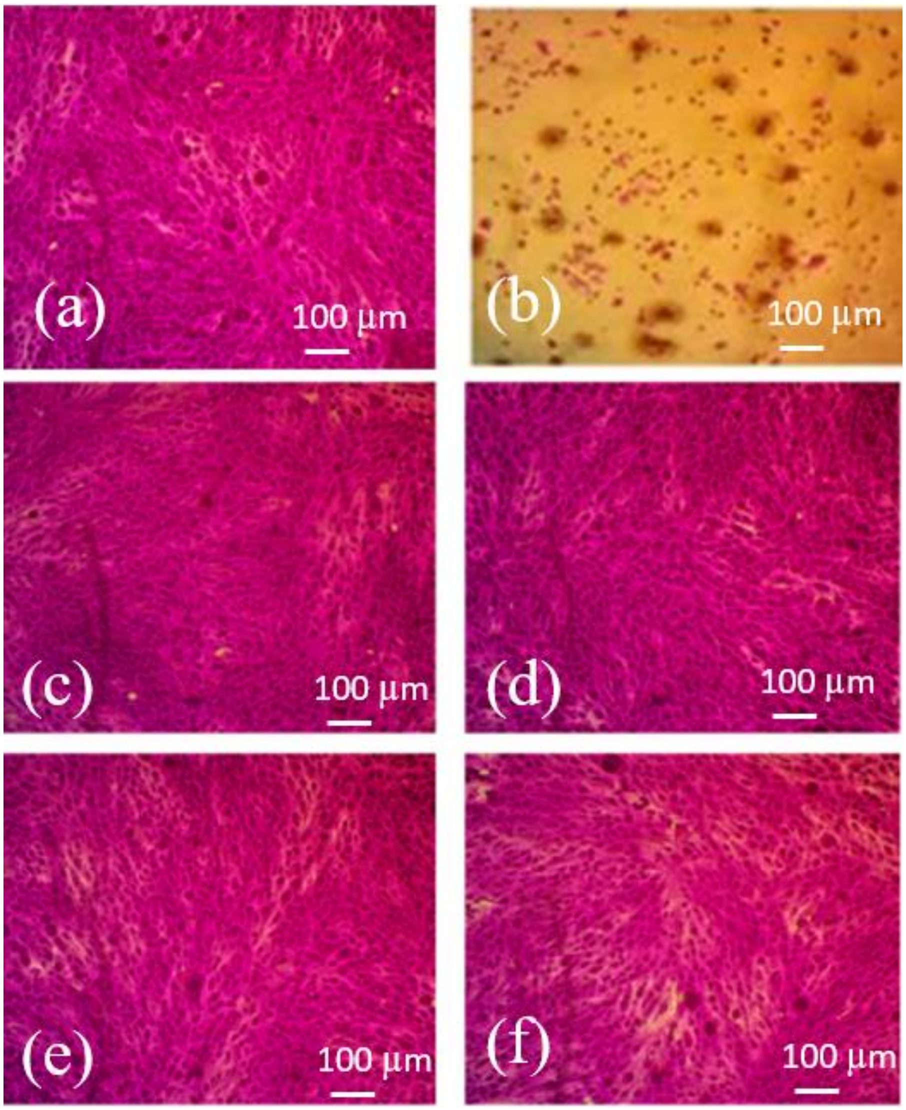

Fig. 8 (a) Morphology of Vero cells of untreated cells (pure sample), (b) image of cells treated with only 10 ug/ml DOX, and Vero cells after being treated with 1 mg of (c) CHBZ1, (d) CHBZ2, (e) CHBZ3, and (f) CHBZ4 samples.

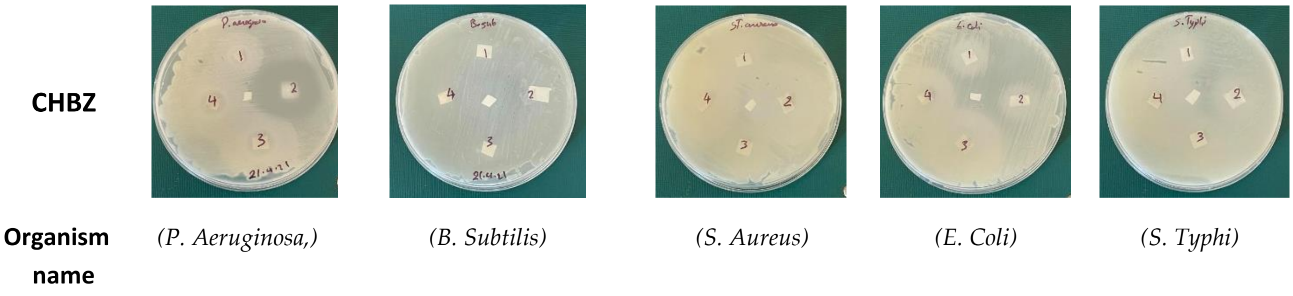

Fig. 9 Results of antibacterial testing for nanocomposites CHBZ1-4 against five pathogenic bacterial strains *(Pseudomonas. Aeruginosa, Bacillus. Subtilis, (Bacillus. Subtilis, Escherichia. Coli, and Salmonella. Typhi).* Only Formula CHBZ2 Pic No.1. shows antibacterial activity against *Pseudomonas. Aeruginosa,* while other formulas do not exhibit any activity towards the rest of the strains.

based on cellulose acetate, hydroxyapatite, and bioglass with different loading of ZrO_2 was synthesized with the solvent casting method. The target materials were also characterized by different techniques including FTIR, SEM with EDX analyses, thermal analyses (TGA, DTA), and XRD. Also, the mechanical, contact angle and bioactivities measurements have been conducted for these synthesized nanocomposites. It could be observed that with the increase of the ZrO_2 content, the microhardness is increased from 245.8 MPa at 1.3 wt% to 405.5 MPa at 11.76 wt% of ZrO_2 as compared with those which are unmodified, show low microhardness (69.4 MPa), and lead to a high value of modulus. It can be revealed that because of the characterization of the prepared samples, all the contributed composite nanoparticles have appeared, and a semi-crystalline pattern has been detected. Moreover, the results clarified that the increase in the ZrO_2 content has led to an improvement in the two mechanical and thermal properties and a decrease in the contact angle. From our results, we believe that the proposed synthesized nanocomposite could serve as a potential candidate material for orthopedic and dental implants. Under the conditions of this in vitro study, using these novel Nanocomposite materials will be safe. Particularly, it did not show cytotoxic effects on normal mammalian cells, which is important for clinical applications of these materials.

Supporting information

Applicable.

Conflict of interest

There are no conflicts to declare.

References

[1] R. Golubevas, Z. Stankeviciute, A. Zarkov, R. Golubevas, L. Hansson, R. Raudonis, A. Kareiva, E. Garskaite, *Materials Advances*, 2020, **1**, 1675-1684, doi: 10.1039/d0ma00498g.

[2] H. Wang, P. F. Hou, *Science of Advanced Materials*, 2020, **12**, 1634-1641, doi: 10.1166/sam.2020.3907.

[3] Y. Y. Li, W. W. Jing, J. H. Wang, J. F. Li, *Science of Advanced Materials*, 2020, **12**, 1213-1224, doi: 10.1166/sam.2020.3767.

[4] K. Rezwan, Q. Z. Chen, J. J. Blaker, A. R. Boccaccini, *Biomaterials*, 2006, **27**, 3413-3431, doi: 10.1016/j.biomaterials.2006.01.039.

[5] Y. Du, J. L. Guo, J. Wang, A. G. Mikos, S. Zhang, *Biomaterials*, 2019, **218**, 119334, doi: 10.1016/j.biomaterials.2019.119334.

[6] B. Conrad, C. Hayashi, F. Yang, *ACS Biomaterials Science & Engineering*, 2020, **6**, 3454-3463, doi: 10.1021/acsbiomaterials.9b01792.

[7] V. Guarino, F., Causa, L. Ambrosio, *Journal of Applied Biomaterials & Functional Materials*, 2007, **5**, 149-157, doi: 10.1177/2280800007005003.

[8] J. Sun, Y, Zhang, Y. Hu, Q. Yang, *Science of Advanced Materials*, 2020, **12**, 1814-1823, doi: 10.1166/sam.2020.3857.

[9] H. Algarni, I. Alshahrani, E. H. Ibrahim, R. A. Eid, M. Kilany, H. A. Ghramh, M. Reben, E. S. Yousef, *Science of Advanced Materials*, 2020, **12**, 101-109, doi: 10.1166/sam.2020.3563.

[10] H. E. Skallevold, D. Rokaya, Z. Khurshid, M. S. Zafar, *International Journal of Molecular Sciences*, 2019, **20**, 5960, doi: 10.3390/ijms20235960.

[11] M. Atai, L. Solhi, A. Nodehi, S. M. Mirabedini, S. Kasraei, K. Akbari, S. Babanzadeh, *Dental Materials*, 2009, **25**, 339-347, doi: 10.1016/j.dental.2008.08.005.

[12] J. S. Kim, B. H. Cho, I. B. Lee, C. M. Um, B. S. Lim, M. H. Oh, C. G. Chang, H. H. Son, *Journal of Biomedical Materials Research Part B: Applied Biomaterials*, 2005, **72B**, 284-291, doi: 10.1002/jbm.b.30153.

[13] S. B. Mitra, D. Wu, B. N. Holmes, *The Journal of the American Dental Association*, 2003, **134**, 1382-1390, doi: 10.14219/jada.archive.2003.0054.

[14] L. Li, L.-J. Zheng, *Science of Advanced Materials*, 2020, **12**, 110-115, doi: 10.1166/sam.2020.3599.

[15] C. Gautam, J. Joyner, A. Gautam, J. Rao, R. Vajtai, *Dalton Transactions*, 2016, **45**, 19194-19215, doi: 10.1039/c6dt03484e.

[16] E. N. Bifari, S. Bahadar Khan, K. A. Alamry, A. M. Asiri, K. Akhtar, *Current Pharmaceutical Design*, 2016, **22**, 3007-3019, doi: 10.2174/1381612822666160316160016.

[17] P. Gouma, R. Xue, C. P. Goldbeck, P. Perrotta, C. Balázsi, *Materials Science and Engineering: C*, 2012, **32**, 607-612, doi: 10.1016/j.msec.2011.12.019.

[18] K. Zhang, Q. Van Le, *Journal of Composites and Compounds*, 2020, **2**, 10-17, doi: 10.29252/jcc.2.1.2.

[19] R. Odermatt, M. Par, D. Mohn, D. B. Wiedemeier, T. Attin, T. T. Tauböck, *Journal of Clinical Medicine*, 2020, **9**, 772, doi: 10.3390/jcm9030772.

[20] C. Hu, J. Sun, C. Long, L. Wu, C. Zhou, X. Zhang, *Nanotechnology Reviews*, 2019, **8**, 396-404, doi: 10.1515/ntrev-2019-0035.

[21] K. Prusty, S. K. Swain, *Journal of Applied Polymer Science*, 2020, **137**, 49284, doi: 10.1002/app.49284.

[22] D. Pan, G. Yang, H. M. Abo-Dief, J. Dong, F. Su, C. Liu, Y. Li, B. Bin Xu, V. Murugadoss, N. Naik, S. M. El-Bahy, Z. M. El-Bahy, M. Huang, Z. Guo, *Nano-Micro Letters*, 2022, 14, 118, doi: https://doi.org/10.1007/s40820-022-00863-z.

[23] M. Gad, A. S. ArRejaie, M. S. Abdel-Halim, A. Rahoma, *International Journal of Dentistry*, 2016, **2016**, 1-6, doi: 10.1155/2016/7094056.

[24] L. Bacakova, J. Pajorova, M. Tomkova, R. Matejka, A. Broz, J. Stepanovska, S. Prazak, A. Skogberg, S. Siljander, P. Kallio, *Nanomaterials*, 2020, **10**, 196, doi: 10.3390/nano10020196.

[25] P. Kumar, V. Kumar, R. Kumar, R. Kumar, C. I. Pruncu, *Journal of the Mechanical Behavior of Biomedical Materials*, 2020, **109**, 103854, doi: 10.1016/j.jmbbm.2020.103854.

[26] S.-H. An, T. Matsumoto, H. Miyajima, A. Nakahira, K. H. Kim, S. Imazato, *Dental Materials*, 2012, **28**, 1221-1231, doi: 10.1016/j.dental.2012.09.001.

[27] T. Bian, L. Wang, H. Xing, *Materials Chemistry and Physics*, 2021, **267**, 124616, doi: 10.1016/j.matchemphys.2021.124616.

[28] J. R. Jones, *Acta Biomaterialia*, 2013, **9**, 4457-4486, doi: 10.1016/j.actbio.2012.08.023.

[29] S. Zidan, N. Silikas, A. Alhotan, J. Haider, J. Yates, *Materials*, 2019, **12**, 1344, doi: 10.3390/ma12081344.

[30] S. U. Hong, Y. S. Cho, S. H. Kim, Y. T. Lee, *Materials Research Innovations*, 2015, **19**, S5-1289, doi: 10.1179/1432891714z.0000000001296.

[31] A. Felipe Jaramillo, S. Riquelme, L. F. Montoya, G. Sánchez-Sanhueza, C. Medinam, D. Rojas, F. Salazar, J. pablo Sanhueza, M. Francisco Meléndrez, *Polymer Composites*, 2019, **40**, 1870-1882, doi: 10.1002/pc.24949.

[32] S. Suleman Ismail Abdalla, H. Katas, J. Y. Chan, P. Ganasan, F. Azmi, M. Fauzi Mh Busra, *RSC Advances*, 2020, **10**, 4969-4983, doi: 10.1039/c9ra08680c.

[33] G. Abdelaziz, H. A. Shamsel-Din, M. O. Sarhan, M. A. Gizawy, *Journal of Labelled Compounds and Radiopharmaceuticals*, 2020, **63**, 33-42, doi: 10.1002/jlcr.3819.

[34] A. Salama, A. Mohamed, N. M. Aboamera, T. Osman, A. Khattab, *Advances in Polymer Technology*, 2018, **37**, 2446-2451, doi: 10.1002/adv.21919.

[35] M. Goswami, A. M. Das, *Carbohydrate Polymers*, 2019, **206**, 863-872, doi: 10.1016/j.carbpol.2018.11.040.

[36] X. He, Z. Wang, D. Wang, F. Yang, R. Tang, J.-X. Wang, Y. Pu, J.-F. Chen, *Applied Surface Science*, 2019, **491**, 505-516, doi: 10.1016/j.apsusc.2019.06.187.

[37] Y. H. Meng, C. Y. Tang, C. P. Tsui, D. Z. Chen, *Journal of Materials Science: Materials in Medicine*, 2008, **19**, 75-81, doi: 10.1007/s10856-007-3107-5.

[38] Y. H. Meng, C. Y. Tang, C. P. Tsui, *Composite Interfaces*, 2010, **17**, 551-558, doi: 10.1163/092764410x513404.

[39] Y. H. Meng, C. Y. Tang, C. P. Tsui, P. S. Uskokovic, *Journal of Composite Materials*, 2010, **44**, 871-882, doi: 10.1177/0021998309349552.

[40] K. Lefatshe, C. M. Muiva, L. P. Kebaabetswe, *Carbohydrate Polymers*, 2017, **164**, 301-308, doi: 10.1016/j.carbpol.2017.02.020.

[41] S. Manafi, F. Mirjalili, R. Reshadi, *Progress in Biomaterials*, 2019, **8**, 77-89, doi: 10.1007/s40204-019-0112-y.

[42] M. Sandhyarani, N. Rameshbabu, K. Venkateswarlu, L. Rama Krishna, *Surface and Coatings Technology*, 2014, **238**, 58-67, doi: 10.1016/j.surfcoat.2013.10.039.

[43] G. Ciobanu, A. Maria Bargan, C. Luca, *Ceramics International*, 2015, **41**, 12192-12201, doi: 10.1016/j.ceramint.2015.06.040.

[44] X. Zhao, X. Chen, L. Zhang, Q. Liu, Y. Wang, W. Zhang, J. Zheng, *Coatings*, 2018, **8**, 357, doi: 10.3390/coatings8100357.

[45] W. Francisco, F. V. Ferreira, E. V. Ferreira, L. De Simone Cividanes, A. D. R. Coutinho, G. P. Thim, *Journal of Aerospace Technology and Management*, 2015, **7**, 289-293, doi: 10.5028/jatm.v7i3.485.

[46] C. Yang, X. Cao, S. Wang, L. Zhang, F. Xiao, X. Su, J. Wang, *Ceramics International*, 2015, **41**, 1749-1756, doi: 10.1016/j.ceramint.2014.09.120.

[47] N. P. Thomas, N. Tran, P. A. Tran, J. L. Walters, J. D. Jarrell, R. A. Hayda, C. T. Born, *Journal of Materials Science: Materials in Medicine*, 2014, **25**, 347-354, doi: 10.1007/s10856-013-5093-0.

[48] V. Chandra, J. Park, Y. Chun, J. W. Lee, I. C. Hwang, K. S. Kim, *ACS Nano*, 2010, **4**, 3979-3986, doi: 10.1021/nn1008897.

[49] Y. Fei, Y. Li, S. Han, J. Ma, *Journal of Colloid and Interface Science*, 2016, **484**, 196-204, doi: 10.1016/j.jcis.2016.08.068.

[50] S. Y. Ju, H. L. Yu, L. Ji, K. Wang, J. X. Jiang, *Science of Advanced Materials*, 2020, **12**, 802-809, doi: 10.1166/sam.2020.3742.

[51] C. Setajit, C. Kongvarhodom, H. Xiao, *Science of Advanced Materials*, 2020, **12**, 212-219, doi: 10.1166/sam.2020.3628.

[52] A. Santamaria-Echart, L. Ugarte, C. García-Astrain, A. Arbelaiz, M. A. Corcuera, A. Eceiza, *Carbohydrate Polymers*, 2016, **151**, 1203-1209, doi: 10.1016/j.carbpol.2016.06.069.

[53] R. A. Ilyas, S. M. Sapuan, M. R. Ishak, *Carbohydrate Polymers*, 2018, **181**, 1038-1051, doi: 10.1016/j.carbpol.2017.11.045.

[54] M. Fan, D. Dai, B. Huang, *Fourier Transform—Materials Analysis*, 2012, **3**, 45-68, doi: 10.5772/35482.

[55] R. M. Sheltami, I. Abdullah, I. Ahmad, A. Dufresne, H. Kargarzadeh, *Carbohydrate Polymers*, 2012, **88**, 772-779, doi: 10.1016/j.carbpol.2012.01.062.

[56] M. Othmani, A. Aissa, A. Grelard, R. K. Das, R. Oda, M. Debbabi, *Colloids and Surfaces A: Physicochemical and Engineering Aspects*, 2016, **508**, 336-344, doi: 10.1016/j.colsurfa.2016.08.078.

[57] M. Srivastava, A. K. Ojha, S. Chaubey, P. K. Sharma, A. C. Pandey, *Journal of Alloys and Compounds*, 2010, **494**, 275-284, doi: 10.1016/j.jallcom.2010.01.008.

[58] A. H. Hashem, A. M. A. Khalil, A. M. Reyad, S. S. Salem, *Biological Trace Element Research*, 2021, **199**, 3998-4008, doi: 10.1007/s12011-020-02506-z.

[59] X. Y. Zhang, X. J. Zhang, Z. L. Huang, B. S. Zhu, R. R. Chen, *Dental Materials Journal*, 2014, **33**, 141-146, doi: 10.4012/dmj.2013-054.

[60] N. Kawai, J. Lin, H. Youmaru, A. Shinya, A. Shinya, *Journal of Dental Sciences*, 2012, **7**, 118-124, doi: 10.1016/j.jds.2012.03.007.

[61] D. O. Njobuenwu, E. O. Oboho, R. H. Gumus, *Leonardo Electronic Journal of Practices and Technologies*, 2007, **10**, 29-38.

[62] Y. Yuan, T. R. Lee, *Berlin, Heidelberg: Springer Berlin Heidelberg*, 2013, 3-34, doi: 10.1007/978-3-642-34243-1_1.

[63] Java-based image processing ImageJ software; website (last accessed on 31/8/2021): https://imagej.nih.gov/ij/download.html.

[64] Biomedical Imaging Group, EPFL, Drop Shape Analysis, website (last accessed on 12/3/2021): http://bigwww.epfl.ch/demo/dropanalysis/.

[65] C. S. Julie Chandra, N. George, S. K. Narayanankutty, *Carbohydrate Polymers*, 2016, **142**, 158-166, doi: 10.1016/j.carbpol.2016.01.015.

[66] C. J. Chirayil, J. Joy, L. Mathew, M. Mozetic, J. Koetz, S. Thomas, *Industrial Crops and Products*, 2014, **59**, 27-34, doi: 10.1016/j.indcrop.2014.04.020.

[67] S. Yadav, P. Singh, R. Pyare, *Ceramics International*, 2020, **46**, 10442-10451, doi: 10.1016/j.ceramint.2020.01.043.

[68] M. A. Hussein, *Journal of Polymers and the Environment*,

2018, **26**, 1194-1205, doi: 10.1007/s10924-017-1023-4.
[69] M. A. Hussein, R. M. El-Shishtawy, A. Y. Obaid, *RSC Advances*, 2017, **7**, 9998-10008, doi: 10.1039/c6ra28756e.

Author information

Nuha Al-Harbi *received her B.Sc. and M. Sc degrees in Physics from Umm Al Qura University, Kingdom of Saudi Arabia in 2003 and 2009, respectively. She joined as a PHD student in laser physics in 2017 at King Abdulaziz University, Kingdom of Saudi Arabia. Recently, she is a lecturer at the Physics Department, Umm Al-Qura University, Kingdom of Saudi Arabia and serving as a member of several scientific and administrative committees, namely, the Administrative Supervision Committee at the Fifth Scientific Conference of the College of Science, Umm Al-Qura University in 2012. Currently, she is developing novel methods to use bioactive glasses in dentistry.*

Prof. Mahmoud Ali Hussein *is a professor of Polymer Chemistry at Chemistry Department, Faculty of Science, Assiut University, Egypt. He obtained BSc in Chemistry and PhD in Organic Polymer Synthesis from Assiut University, Egypt. He got a position at Chemistry Department, King Abdulaziz University (KAU), Jeddah, Saudi Arabia. He got a postdoctoral position in the University of Nice Sophia Antipolis, France and University Sains Malaysia, Malaysia. He visited the school of Industrial technology, University Sains Malaysia and Faculty of Engineering, University of Porto (UP) as visiting researcher. He published +150 ISI papers and numerus number of conference papers (poster and oral presentations). His research interests are in the area of polymer synthesis, characterization and applications for different fields, polymer composites materials, polymer-doped organic and/or inorganic substances for variable industrial as well as biological interests.*

Prof. Yas Al-Hadeethi *received his B.Sc. degree in physics from Al-Mustansiriya University-Baghdad, Iraq, in 1982, the Postgraduate diploma; M.Sc. and Ph.D. in Laser-Physics from Essex University, UK, in 1985,1986 and 1995, respectively. In 1995, Yas joined the Max-Born Institute for nonlinear-optics and short-pulse spectroscopy, Berlin, as postdoc fellow. He joined many Arab and European Universities as professor of physics, chief of researchers and director of national research programs. Yas received several research awards and 54 funded research projects, regional and National shields, medals, scientific awards and decorations. He also acted as principal investigator in more than 40 projects. He worked for HiPER, the European High-Power Laser Energy Research facility for Laser-induced thermonuclear fusion supervising the High Power Laser Research Lab at Milano Bicocca University-Italy. Yas supervised the construction and running of class 100 and 1000 clean rooms equipped with the most sophisticated nano-fabrication and characterizations facilities at King Abdulaziz University. He is a Professor of Laser Physics at the Physics Department, King Abdulaziz University (KAU) and the head of the lithography research group at the Deanship of Scientific research, KAU. Yas collaborated with KAUST, Max-Born Institute, University of California at Riverside, senior scientists at George Washington University etc. He supervised and examined more than 120 PhD and MSc theses in Europe, Arab countries, Malaysia etc. He is also heading many academic and scientific committees and a frequent expert to the International conferences of the Arab Industrial Development and Mining Organization, Associate of the INFN-Italian National Institute of Nuclear Physics (INFN) in 2009, and basic member of the SPIE- The International Society for Photo-Optical Instrumentation Engineers-Washington DC since 1987. His h-index = 21, Highly Cited in Field (8) , Hot Papers in Field (5). Yas published more than 150 papers, approximately, a significantly high number of them at top 5% to 10% Q1 ranking ISI Journals.*

Prof. Ahmad Umar *received his Ph.D. in semiconductor and chemical engineering from Chonbuk National University, South Korea. He worked as a research scientist in Brain Korea 21, Centre for Future Energy Materials and Devices, Chonbuk National University, South Korea, in 2007–2008. Afterwards, he joined the Department of Chemistry in Najran University, Najran, Saudi Arabia. He is a distinguished professor of chemistry and served as deputy director of the Promising Centre for Sensors and Electronic Devices (PCSED), Najran University, Najran, Saudi Arabia. Professor Ahmad Umar is specialized in 'semiconductor nanotechnology', which includes growth, properties and their various high technological applications, for instance, gas, chemicals and biosensors, optoelectronic and electronic devices, field effect transistors (FETs), nanostructure-based energy-harvesting devices, such as solar cells, Li-ion batteries, super-capacitors, semiconductor nanomaterial- based environmental remediation, and so on. He is also specialized in the modern analytical and spectroscopic techniques used for the characterizations and applications of semiconductor nanomaterials. He contributed to the world of science by editing world's first handbook series on Metal Oxide Nanostructures and Their Applications (5-volume set, 3500 printed pages, www.aspbs.com/mona) and handbook series on Encyclopedia of Semiconductor Nanotechnology (7-volume set; www.aspbs.com/esn), both published by American Scientific Publishers (www.aspbs.com). He has published more than 600 research papers in reputed journal with h-index of 76 and i10-index of 380 with total citations of 20673 (According to Google scholar).*